



AIAA 99-2859

An Experimental and Theoretical Analysis of the  
Grid Clearing Capability of the NSTAR Ion  
Propulsion System

Keith D. Goodfellow, Gani B. Ganapathi  
and John F. Stocky

Jet Propulsion Laboratory  
California Institute of Technology  
Pasadena, CA 91109

**35<sup>th</sup> AIAA/ASME/SAE/ASEE Joint Propulsion  
Conference and Exhibit**  
20-24 June, 1999  
Los Angeles, CA

For permission to copy or to republish, contact the American Institute of Aeronautics and Astronautics,  
1801 Alexander Bell Drive, Suite 500, Reston, VA, 20191-4344.

## An Experimental and Theoretical Analysis of the Grid Clearing Capability of the NSTAR Ion Propulsion System

Keith D. Goodfellow, Gani B. Ganapathi and John F. Stocky

*Jet Propulsion Laboratory  
California Institute of Technology  
Pasadena, California*

The capabilities of the grid clearing system for the NSTAR/DS1 ion propulsion system were investigated through a series of experiments and theoretical analysis. A range of stainless steel wire diameters were tested. The system is capable of clearing wires up to 0.15 mm diameter with one pulse. The maximum fiber diameters removed from the DS1 spacecraft prior to launch was well within this capability. Wires up to 0.28 mm diameter could be cleared with several pulses in most cases. In a few cases however, a low resistance short was created that the grid-clear system could not eliminate. As expected, the model suggests that the system is capable of clearing wires diameters that are 1.7 times larger if a 10A current is used instead of 4A, and that the diameters that can be cleared are 2.8 times smaller for molybdenum than for stainless steel.

### Introduction

NASA's 30 cm diameter xenon ion thruster technology is being validated for use in planetary missions by the NASA Solar Electric Propulsion Technology Application Readiness (NSTAR) program. This program is designed to develop the industrial capability to produce flight engine, power processor, and propellant feed system hardware and demonstrate that the technology is mature enough for flight applications. One of the goals of the program is to provide flight managers with sufficient information on performance, reliability and spacecraft interactions to give them the confidence to use the technology.

The technology validation includes a number of ground tests designed to demonstrate engine performance over the required throttling range, characterizing the engine and plume interactions with the spacecraft, and understanding the dominant failure modes. The program includes 4 long-duration ground based tests and in-flight validation of the xenon ion

thruster technology on the Deep Space 1 (DS1) spacecraft.

One of the possible failure mechanisms for the thruster is a short between the accelerator grids. Early in the mission, potential shorting debris would be from contaminants remaining from the spacecraft assembly and processing. Later in the mission the most likely source of shorting materials would be from flakes formed within the thruster. Erosion within the discharge chamber deposits material on surfaces that may build up to a sufficient thickness that it may flake off. The NSTAR Power Processing Unit (PPU) contains a system that is designed to clear these shorts. This paper discusses the capabilities of this system. Descriptions of the development and performance characteristics PPU and the Digital Control Interface Unit (DCIU) are presented in References 1-3.

An indication that a short exists between the grids is when the system experiences a large number of consecutive recycles. A recycle event occurs when the PPU senses an over-current in either the accelerator grid current or the beam current. For the DS1 system the limits are

voltage system sees the system as shorted but the lower voltage grid-clear circuit sees it as open. The limited amount of energy available also limits the amount of potential damage to the system for this technique, but it may require a lot of pulses and therefore a lot of time.

The third option is to use the special grid-clear circuit built into the NSTAR hardware[3]. The grid-clear circuit for the DS1 configuration is shown in the functional block diagram presented in Fig. 1. The discharge power supply is used to provide the current for the grid-clear. The negative side of the discharge power supply (Cathode Common) is connected to the screen grid within the thruster. For grid-clear operations, the positive side of this supply is connected to the accelerator grid through the grid-clear relay. During the grid-clear operation, the relay is closed a few seconds prior to switching on the power supply and is opened after the supply is switched off. The grid clear system produces a 3.85 A, 30 second duration square pulse with a rise time of about 4 seconds. A typical voltage and current profiles into a 1.1 Ohm resistive load are shown in Fig. 2.

The potential danger with this technique is that the debris may become firmly attached to the grids and form a low resistance short. The lower resistance limits the amount of energy that can be applied to the material and therefore severely limits the system ability to clear the short. This effect was observed in the experiments in this study and are discussed below.

### Modeling

Prior to conducting grid clear experiments, a model was developed to help the process. The primary goal of the modeling effort was to guide the grid clear testing process by establishing limits of contaminant sizes that can be cleared by the DS1 grid clear system.

The model was developed assuming a wire geometry for the grid contaminant. No attempt was made to duplicate flight contaminant, which is unknown. Hence any 3-d flake geometry was avoided. The rationale was that sufficient information would be determined by using a wire geometry to make a meaningful decision and yet avoid the complexities associated with 3-d modeling. The model geometry is shown in Fig. 3.

The model involves solving a second order partial differential equation-boundary value problem in one dimension for transient heat transfer. Contact resistance is accounted for as a variable and is considered to be evenly shared between the two wire end nodes. This model is expanded upon in the next section.

The governing equation for the heat transfer problem is shown below:

$$A_{cs}\rho c_p \frac{\partial T(x,t)}{\partial t} = A_{cs}k \frac{\partial^2 T(x,t)}{\partial x^2} - 2\pi r \epsilon \sigma (T(x,t)^4 - T_{external}^4) + I^2(t) \frac{\gamma(T(x,t))}{A_{cs}} \quad (1)$$

where,

$A_{cs}$  = cross-section area of wire (m<sup>2</sup>)

$\rho$  = density of wire (kg/m<sup>3</sup>)

$c_p$  = heat capacity (J/kg-K)

$T(x,t)$  = temperature of wire at a distance x from end and at time t (K)

$k$  = thermal conductivity of wire (W/m-K)

$\epsilon$  = emissivity of wire surface (dimensionless)

$\sigma$  = Stefan-Boltzmann constant (5.669 x 10<sup>-8</sup> W/m<sup>2</sup>-K<sup>4</sup>)

$T_{extern}$  = external temperature (K)

$I(t)$  = current from power supply (A)

$\gamma(T(x,t))$  = resistivity of wire (Ohm-m)

In the model above, the term on the left is the rate of accumulation of heat within a node. The first term on the right is the net heat conducted in across the cross section area, the second term is the heat radiated out to ambient, and the third term corresponds to internal heating due to passage of electrical current.

The boundary conditions for the problem were specified to be  $T(0,t) = T(l,t) = 294K$ , where l is the inter-grid distance and is 0.66 mm for DS1. The thermal masses of the grid grids are so much larger than the wire that the boundary temperatures will remain essentially constant even when the wire heats up on passage of current and the heat soaks back into the grids.

The model was developed to account for the latent heat of sublimation. Thus, the nodes are set up to lose mass during the sublimation process when the temperature of the node reaches the sublimation temperature. This causes a phenomenon called "necking", which has a

trying to extend this conclusion for very low pressures as the following analysis will indicate.

For solid(s) and gas(g) phases in equilibrium,  $\Delta G_{sg} = \Delta H_{sg} - T_{\text{sublim}} \Delta S_{sg} = 0$ . From the Clausius-Clapyron equation, we have

$$\frac{dP}{dT} = \frac{\Delta S_{sg}}{\Delta V_{sg}} = \frac{\Delta H_{sg}}{T \Delta V_{sg}} \quad (2)$$

If we assume  $\Delta V_{sg} \sim V_g$ , then

$$\frac{d(\ln P)}{dT} = \frac{\Delta H_{sg}}{RT^2} \quad (3)$$

Thus, at very low pressures, the large  $d(\ln P)/dT$  will offset the low sublimation temperatures, and will result in higher heats of sublimation. These gross thermodynamic conclusions need to be examined in greater detail using more a refined kinetic modeling approach; this is not in the scope of the present discussion.

Due to the low pressures, another important effect is the absence of a liquid phase at any temperature. Thus, theoretically no true welding is possible, and the contact resistance can be modified by thermal cycling. The implication of this is that regardless of the initial contact resistance, it should be possible to clear any contaminant provided it is of a size smaller than the maximum.

The finite element model for solving the differential equation (1) used 50 grids. A choice of 50 grids was determined by trial and error to be optimal in terms of maintaining the desired fidelity and keeping computational costs down. The 1st and 50th grid were assumed to be at fixed temperature to satisfy the boundary conditions. The contact resistance was assumed to be shared evenly between the 2nd and 49th grid. Since the initial temperature for the entire wire was the same as the end points, the problem was of an initial value type with specified boundary conditions; the only constraint was in being able to choose a step size that would not cause instabilities in the solution. The optimal step size was determined by trial and error to be in the order of 7-10 microseconds. The DS1 PPU current profile as a function of time was modeled. Based on experiments with resistive loads, it was possible to model the current as:

- 1) if total resistance < 11.7 ohm  
if time < 0.03 sec,  
current =  $2.5 * \text{time} / 0.03$   
if time  $\geq 0.03$  sec,  
current =  $2.5 + 1.34 * (1 - \exp(\text{time} / 0.82))$
- 2) if total resistance > 11.7 ohm  
if time < 0.03 sec,  
current =  $(44.8 / \text{resistance}) * \text{time} / 0.03$   
if time > 0.03 sec,  
current =  $44.8 / \text{resistance}$

Since the maximum voltage that can be supplied is 44.8 V, the current falls below the maximum value of 3.85 A when the total resistance is above 11.7 ohms. The total resistance is the sum of bare wire resistance and the contact resistance. In the model, the lead wire resistance was neglected. The total value was estimated to be less than 0.2 Ohms and will not change the model results.

Since the contact resistance is not amenable to easy analysis, the results were expressed in terms of the upper and lower limits of initial total resistance that bound the region where the wire can be cleared with the grid clear approach for the range of wire radii. As mentioned previously, the initial total resistance consists of the contact resistance and the bare wire resistance.

With the intent of keeping the model simple, the contact resistance was initially treated as a variable in two nodes only and the "necking" phenomenon was neglected. The model was then exercised for wire radii ranging from 5 microns to 0.16 mm. The results with annotations are shown behind in Fig. 6.

On examining Fig. 6, it can be seen that there are three primary zones that characterize the grid clear boundary. Two of them, the "zero contact resistance" zone (lower left line) and the "voltage limited" zone (upper line) are well defined and have temperature profiles as shown in the annotations included with the graph. The third, named the "finite contact resistance" zone is a transition zone where the temperature profiles at time of clearing varies depending on many factors.

In the "zero contact resistance" zone, the resistance of the bare wire varies as the inverse of area, and the PPU supplied current will always clear the wire. The center of the wire will reach the highest temperature first and the temperature profile will be parabolic as shown in Fig. 6

"necking". Due to time constraints the simulation was not continued for cases where more than one grid clear command could be issued. The actual duration of a grid clear command is 30 seconds, however determination of each point in Fig. 9 takes several hours.

During the grid clear process, the nodes that reach sublimation temperature remain at that temperature and the node radius starts decreasing as a result of the sublimation process. This is best illustrated by examining Fig. 10 for a wire of initial radius 75  $\mu\text{m}$ .

From Fig. 10 we observe the following. At some time  $t = 0.3$  sec, the temperature profile within the wire is parabolic with a maximum around 1530  $^{\circ}\text{C}$ ; the radii at all nodes with the exception of the 1<sup>st</sup> and last nodes (which are at room temperature) are same at approximately 72  $\mu\text{m}$ . At a later time,  $t = 0.7$  sec, most of the interior nodes are at sublimation temperature; however, since the middle node reached this temperature before the rest, the radius of this node is the smallest, showing the impact of sublimation. In the simulation for this wire radius, it took approximately 750 msec to clear the wire.

## Experiments

The experiments were designed to characterize the capabilities of the NSTAR PPU system into simulated grid shorts. The main goals were to determine how large of a piece of debris that the system could clear, and whether the attempted grid clears modify the contact resistance between the debris and the grids. In particular, would these attempts locally attach/weld the debris to the grid forming a low impedance short. Such a low impedance short would be difficult to clear due to the limited Ohmic heating. ( $I^2R$  where  $I = 3.85\text{A}$  and constant). In addition the effect of variations in the contact resistance between the wires and the test fixture were investigated for comparison with the model.

A schematic of the test configuration is shown in Fig. 11. Illustrations of the two fixtures were used to hold the test samples are shown in Fig. 12. The first fixture consisted of two molybdenum grid segments from a previous thruster attached to a positioning system that was used to set the correct grid gap. The sample was laid in the holes of the grid segments. Therefore the only contact force between the sample and the

grid pieces was the weight of the sample. In the second test fixture the samples were held between two 3.18 mm thick molybdenum plates with a pair of screws as shown in Fig. 12. The screws allow the loading or contact resistance to be varied. This was done primarily to match the predictions of the model. The test fixtures were placed in a vacuum chamber and evacuated to less than 1 mTorr using a mechanical vacuum pump.

For the test procedure, the samples were placed in both fixtures and the screws were adjusted on the clamp fixture to get the desired contact resistance. In practice, resistances of 0.1 Ohm to 10's of Ohms were easy to achieve. Higher resistances were more difficult to achieve. The values tended to be either shorted ( $<10$  Ohms) or open ( $>40$  Mohm) depending on how the wire was touching. The system was then pumped down to less than 1 mTorr for about 1 hour and was purged with argon 3 or 4 times. The initial resistance was measured using a Fluke 87 DVM to determine if the pump-down had changed the contact resistance. The fixture was then connected to the PPU system and the digital oscilloscope was initialized. A grid clear command was then sent to the DCIU and the sample was observed. Typically the wire sample would glow like a light bulb filament. Following the grid clear pulse, the system was disconnected from the PPU and the resistance was again measured. The sequence was then repeated until either the sample had been cleared or a "hard-short" existed and the test was declared a failure.

Stainless steel wires were used for the initial set of tests. Wire provided a consistent and constant cross-section for the test samples and was easier to model. Stainless steel is a possible contaminant from manufacturing and ground handling, and samples were readily available in a variety of sizes. Future tests will use additional materials (molybdenum, aluminum and carbon) and thin rectangular cross-sections that are more representative of flakes.

## Experimental Results

Measuring the initial resistance with the DVM was found to have little correlation with the test results. These measurements tended to be either shorted ( $<10$  Ohms) or open ( $>40$  MOhm). A better measure of the initial resistance was from the current and voltage traces recorded on the oscilloscope at the initiation of the current pulse. Typically two types of profiles were

evaporates at the highest temperature location. This in-turn reduces the cross-sectional area, which increases the local current density. The higher current density produces a higher temperature and so forth until the wire reaches a critical diameter that the 4 A current is capable of clearing. There is significant scatter in the number of attempts needed to clear the larger wire diameters. For example, for the 0.25 mm wires, the number of attempts ranged from 1 to 18. This indicates that the variations in the contact can have a significant effect on the results.

Adding the effect from necking to the model provides a better correlation with the experimental data. Time constraints prevented examining this effect for all of the wire diameters considered.

The vertical line indicates the maximum fiber diameter size from the tape-lift-off samples taken from the DS1 spacecraft prior to launch. Only the fiber sizes are known since no analysis of the material types was performed. This maximum fiber size falls well within the system capabilities for clearing stainless steel fibers on the first try.

### Observations

Some of the tests that the DCIU indicated as successful grid-clears were not completely successful. That is, the current during the grid-clear pulse dropped below the threshold so that the system considered it successful. However, when another grid-clear command was sent, the wire would begin glowing again. The first pulse probably broke the wire loose so that the resistance increased enough for the current to drop off. However, when the voltage was applied again, it would break down and begin conducting again. This is probably a result of thermal deformation in the system. That is, the wire would break when it was hot and then make contact again once the system has cooled off. Typically there was about 5 minute delay between tests to print out the oscilloscope data.

Most of the wires that blew did so at the midpoint in the wire (15 of 19), where the highest temperature were expected. Two blew near the contact indicating that in these cases the highest temperature was at the contact due to a higher contact resistance. Two of the samples fell out of the fixtures during the chamber venting process.

During the tests the start circuit was used 7 times to convert "open" circuits to lower resistances for the grid clear circuit. That is, the grid clear circuit would see an open circuit but the higher voltages in the start circuit would see a short. The application of the start circuit high voltage would locally attach the wire sufficiently enough for the next application of the grid-clear circuit to see the short.

Two possible failure situations exist for clearing grid shorts. If a hard short exists, then the low resistance prevents sufficient heating from the grid-clear circuit to remove the material. Possible solutions would be to use additional grid-clears or thermal cycling to loosen the material sufficiently that either the system will start or that the contact resistance is sufficiently high enough for following grid-clear pulses to remove it. The other possible failure is from a "partially open" circuit. In this case the grid-clear circuit does not have sufficient voltage to breakdown across the gap and initiate current flow, but the high voltage start circuit still sees sufficient current draw to indicate that a short exists. Possible solutions are to use additional starts to either locally attach the material so that the grid-clear circuit may be used, or to slowly eat away at the material until the gap is large enough for normal engine operation. Thermal cycling could also be used to either dislodge the material, or modify so that sufficient contact could be made between the grids that the grid-clear circuit could be used.

### Future Work

Future tests will be performed with additional materials such as aluminum and molybdenum, and with specimens with rectangular cross-sections. The nonaxisymmetric samples will better represent flakes that will form in the later part of the mission. The modeling effort will further investigate the effect of necking on the wires samples, and the effects of localized attachments at the contacts with the grid surfaces. The current model assumes that the ends of the wire contact the grids over the entire cross-sectional area. The actual contact area is probably much less. Reducing the contact area will reduce thermal loss to fixture and therefore reduce energy need to reach the critical sublimation temperature for a given current. This should further improve

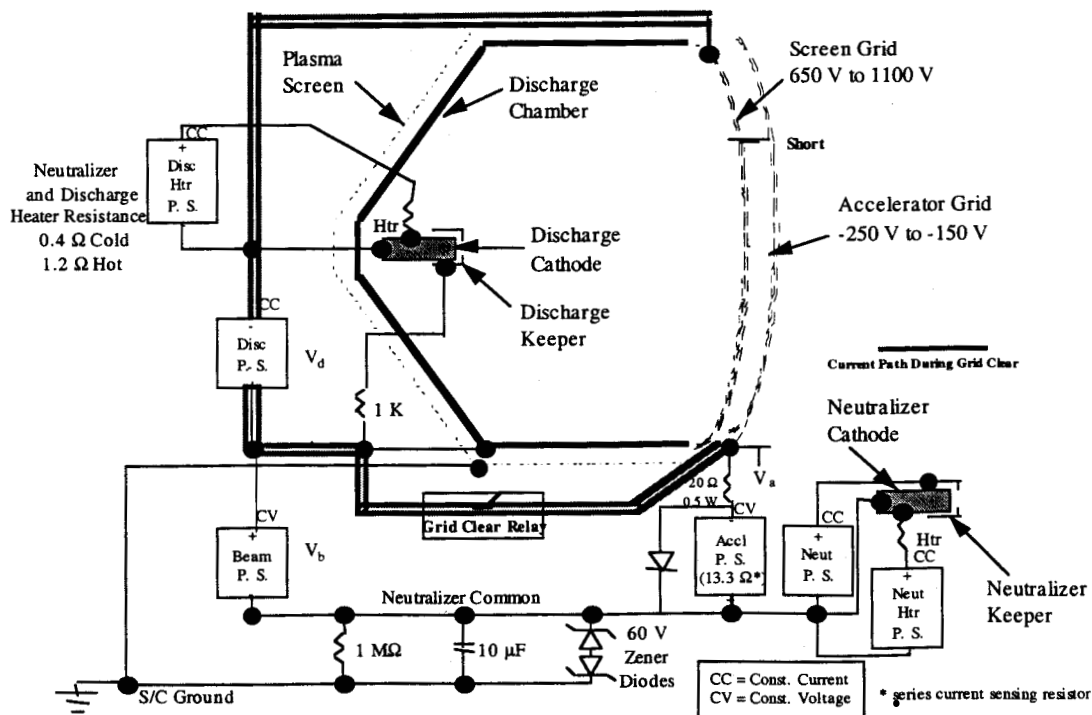


Figure 1. NSTAR thruster and PPU functional block diagram.

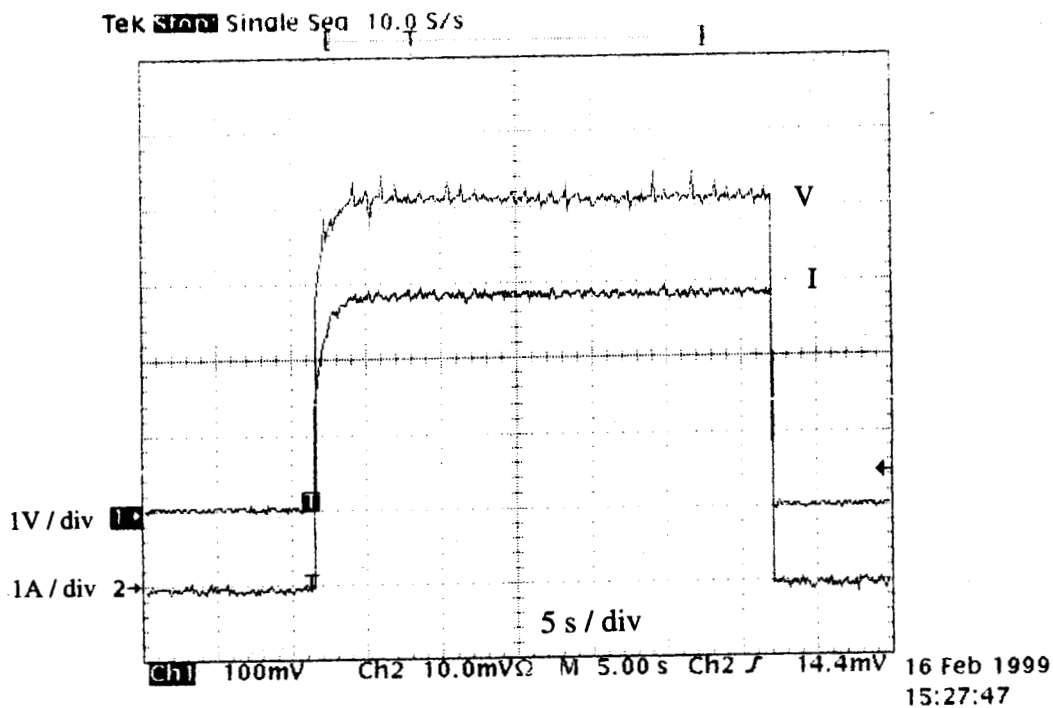


Figure 2. Current and voltage profiles into a 1.1 Ohm resistive load.

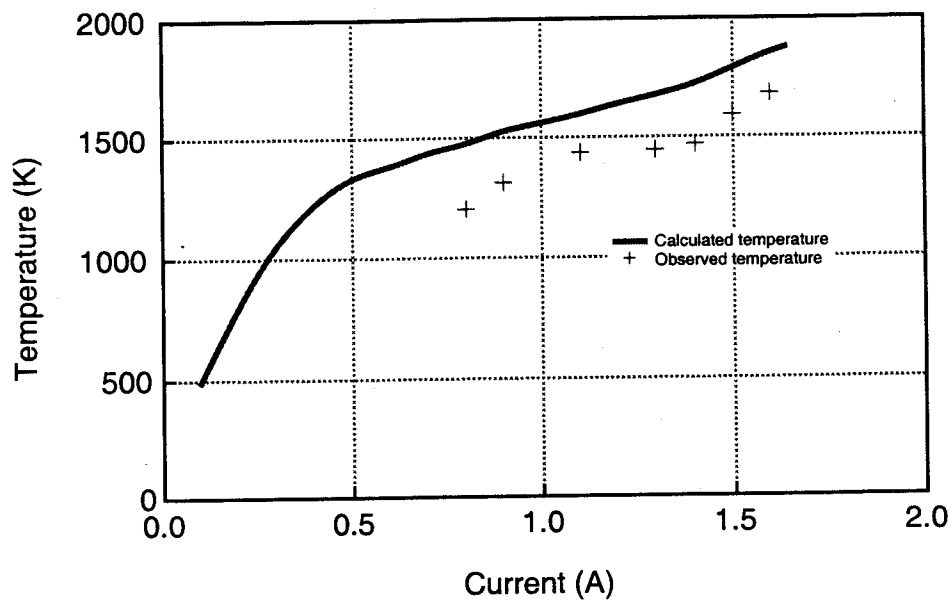


Figure 5. Measured and calculated temperatures for verifying sublimation temperature.

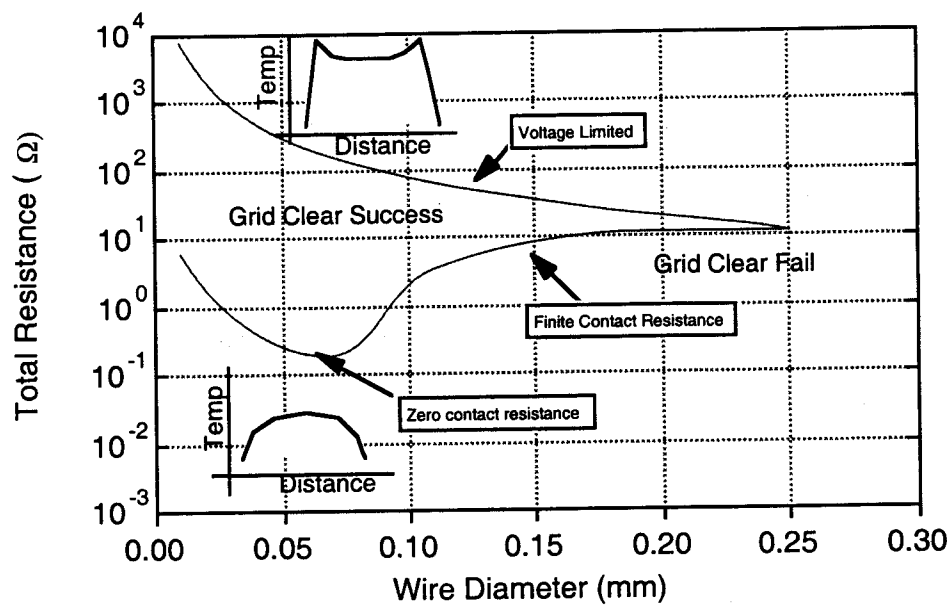


Figure 6. JPL grid-clear model predictions.



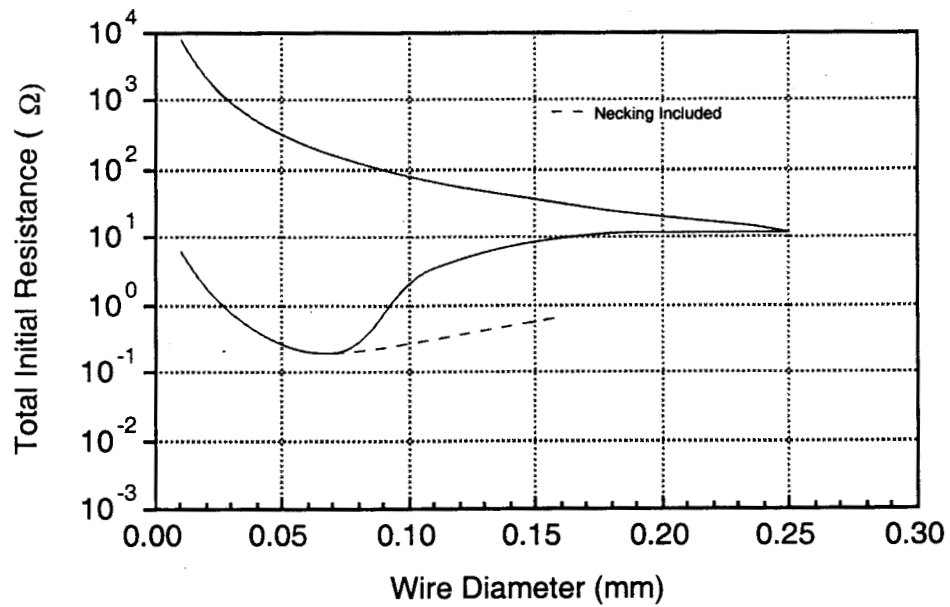


Figure 9. Modified grid clear model for stainless steel with “necking” included.

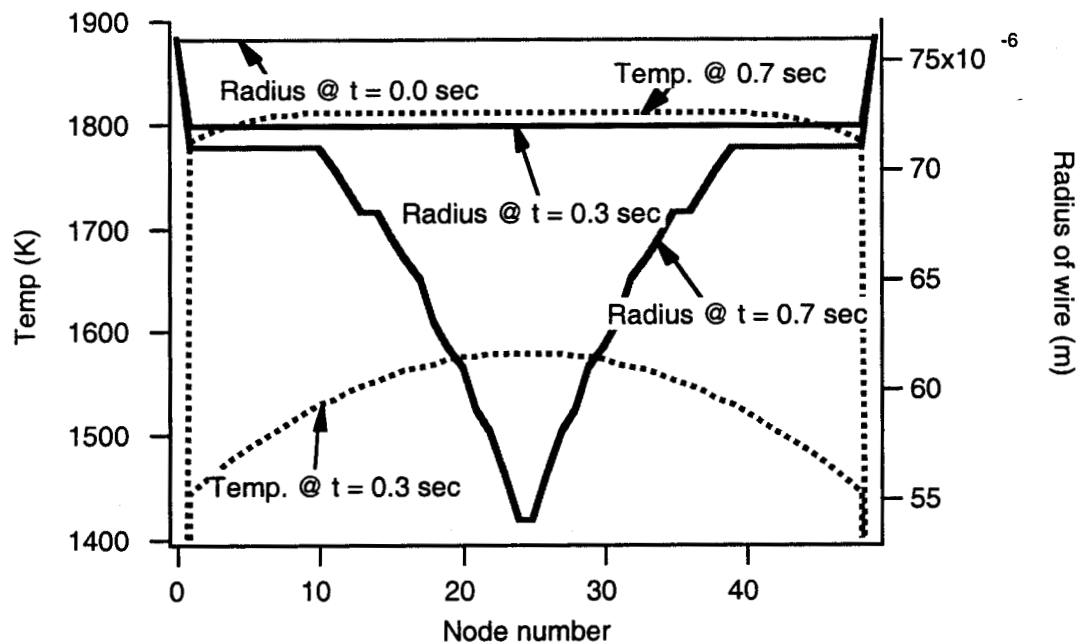


Figure 10. Temperature and radius profiles along wire at different times.

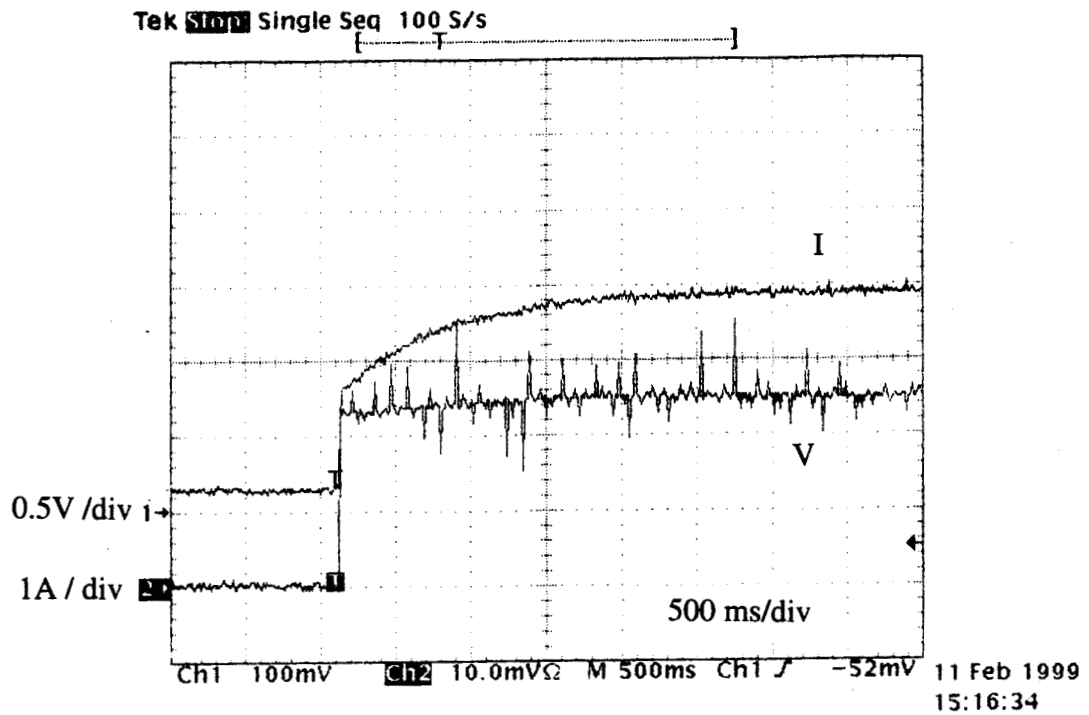


Figure 13. Grid-Clear circuit characteristic on a low resistance short.

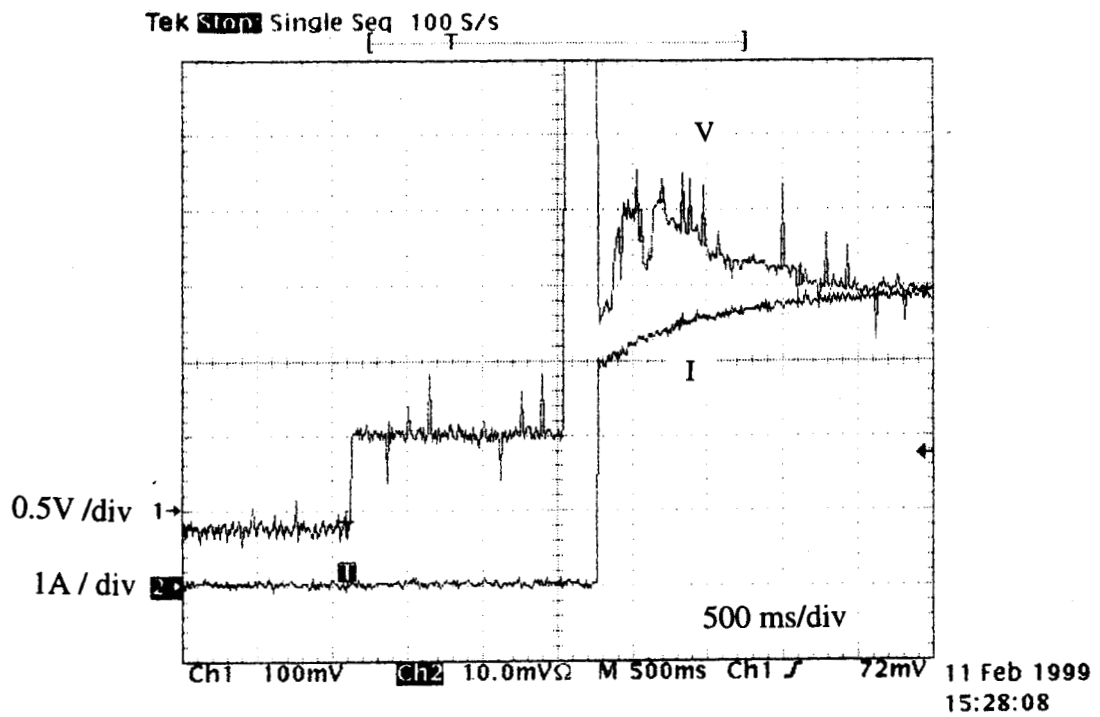


Figure 14. Grid-Clear circuit characteristic on a high resistance short.

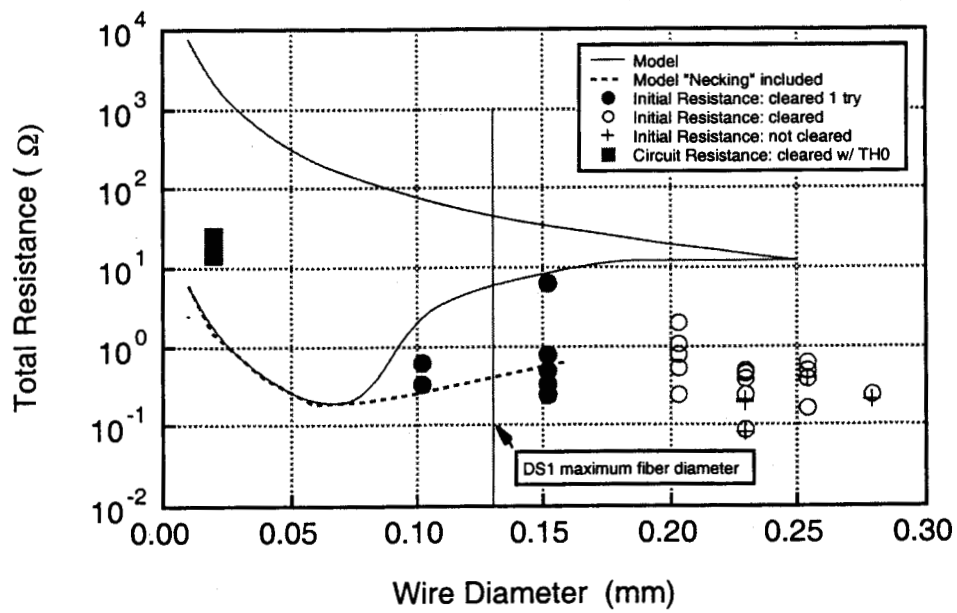


Figure 16. Comparison of numerical and experimental results with all initial resistance values.

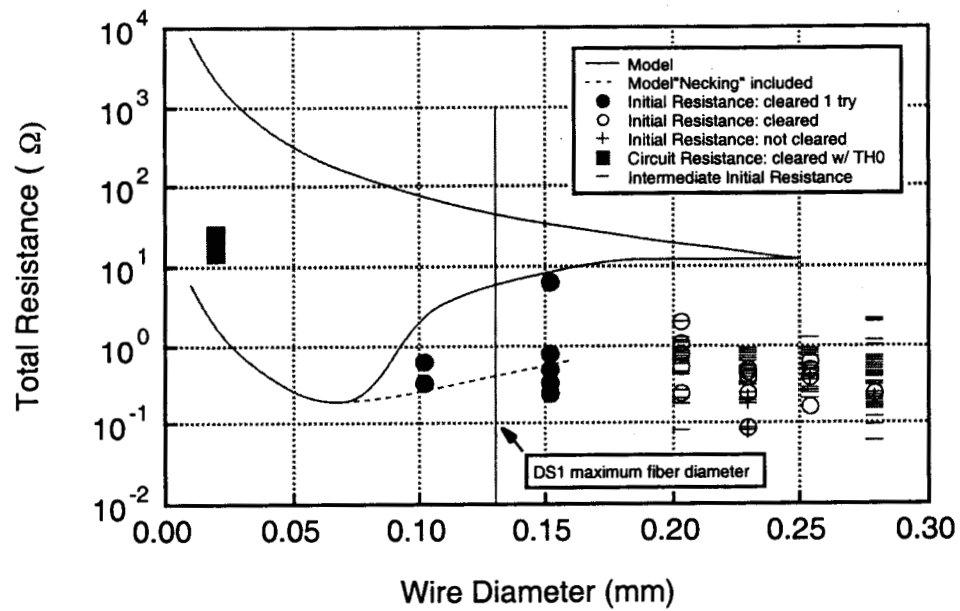


Figure 17. Comparison of numerical and experimental results with all initial resistance values.